High-Performance Hyperentanglement Generation and Manipulation Based on Lithium Niobate Waveguides

Yiwen Huang,[1,‡] Juan Feng,[1,‡] Yuanhua Li,[1,2,*] Zhantong Qi,[1] Chuangyi Lu,[1] Yuanlin Zheng ◉,[1,3] and Xianfeng Chen ◉[1,3,4,5,†]

[1]*State Key Laboratory of Advanced Optical Communication Systems and Networks, School of Physics and Astronomy, Shanghai Jiao Tong University, Shanghai 200240, China*
[2]*Department of Physics, Jiangxi Normal University, Nanchang 330022, China*
[3]*Shanghai Research Center for Quantum Sciences, Shanghai 201315, China*
[4]*Jinan Institute of Quantum Technology, Jinan 250101, China*
[5]*Collaborative Innovation Center of Light Manipulation and Applications, Shandong Normal University, Jinan 250358, China*

Here, we demonstrate the generation and manipulation of hyperentanglement in polarization and time-energy degrees of freedom. The hyperentangled photon pairs are generated by cascaded second-harmonic generation and spontaneous parametric down-conversion processes in a high-efficiency periodically poled lithium niobate (PPLN) waveguide in a fiber Sagnac loop. The states achieve the maximum value of Clauser-Horne-Shimony-Holt Bell inequality of $S = 2.76 \pm 0.03$ with two-photon interference visibility of higher than 99% for polarization entanglement and the Franson-type two-photon interference visibility of 98.5% for time-energy entanglement. In addition, the polarization maximally entangled states can be fast switched to each other by using a PPLN on insulator chip through the electro-optic effect. After the entanglement manipulation, the two-photon interference visibility for polarization entanglement is still higher than 97% while keeping the quantum characteristics of time-energy degrees of freedom maintained. Our system paves a way toward reducing the complexity of quantum systems and has potential applications in many quantum-information tasks like fast superdense coding and teleportation.

I. INTRODUCTION

As the paradigmatic quantum-mechanical resource, quantum entanglement has become the key ingredient in the rapidly expanding field of quantum-information science [1]. Hyperentanglement in multiple degrees of freedom (DOFs) can encode more qubits per transmitted photon [2] and significantly increases channel capacity [3], promising in many quantum-information applications such as entanglement distillation [4], quantum dense coding [5,6], and superdense teleportation [7,8]. For a photonic system, quantum entanglement can be encoded in various DOFs, such as polarization [9], time energy [10], path [11], and orbital angular momentum [12]. Among these DOFs of photons, polarization and time energy are most commonly used in long-distance fiber-based quantum tasks. Time-energy entanglement shows intrinsic robustness for propagation through long-distance fiber

[10], while polarization-entangled states have been wildly used in quantum-information tasks, such as quantum key distribution (QKD) [13], quantum teleportation [14,15], dense coding [5,6], and quantum computation [16]. Hyperentanglement in these two DOFs has great potential for long-distance quantum-information applications.

Nowadays, constructing practical quantum networks has become a hot topic, among which polarization and time-energy entangled sources play a role [17–21]. When scaling up quantum registers, a compact hyperentangled source in these two DOFs that can provide enough photon pairs in the communication band become essential for constructing a large-scale quantum network. Owing to the compatibility with integrated optics and the ability of coiling to a compact size, fiber-based entangled sources have attracted much attention in recent years [22]. Fiber-based polarization and time-energy entangled sources have been achieved via a spontaneous four-wave mixing process in the silicon microring cavity [23] or dispersion shifted fiber [24]. However, it is not easy for the silicon microring cavity to generate photon pairs covering all the wavelength of the communication band due to the large free spectral

___

*lyhua1984@jxnu.edu.cn
†xfchen@sjtu.edu.cn
‡These authors contributed equally to this work.

range of the cavity mode [23]. And the dispersion shifted fiber needs to be cooled to a low temperature through a liquid helium bath or a liquid nitrogen bath to reduce the Raman-noise photon-generation rates [24], which makes the whole system complicated. An effective approach to overcome these limitations is to adopt photonic integrated circuits, e.g., high-efficiency waveguide structures [25–27]. A waveguide-based spontaneous parametric down-conversion (SPDC) process can generate photon pairs of high spectral brightness, broad spectral range, and very low noise background [28,29]. It is extremely beneficial to construct hyperentangled sources in these two DOFs by using a high-efficiency waveguide.

On the other hand, high-fidelity quantum operations, like precise manipulation of polarization entangled state, represent a fundamental prerequisite for many quantum-information technologies [30]. Particularly in superdense coding, the precise manipulation of polarization entanglement is an indispensable part for encoding the quantum information and performing the complete Bell-state measurement [5,6,31]. So far, a variety of progresses have been achieved in single-photon polarization manipulation [32–35]. Silicon photonic chip has been applied in a measurement-device-independent QKD system [35]. High-speed electro-optic (EO) effects in silicon often rely on electronic doping, which faces stringent trade-offs between voltage, bandwidth, and optical losses [36], and thus is not suitable for performing quantum operation to maximally entangled states. To date, there are still fewer studies on the fast manipulation of the polarization entangled state.

Here, we report on the generation and manipulation of hyperentanglement in polarization and time-energy DOFs with high performance. The hyperentanglement is generated by cascaded second-harmonic generation (SHG) and SPDC processes in a high-efficiency PPLN waveguide. The entangled source achieves the fidelity of the polarization state of higher than 98% and the visibility of Franson-type two-photon interference fringes of 98.5% for time-energy entanglement. Then, the manipulation of polarization entangled state is implemented on a PPLN-on-insulator (PPLNOI) chip through the transverse EO effect, with the advantages of integration, low drive voltage, as well as fast-speed response. Our high-performance system has potential applications in high-dimensional quantum-information tasks like fast superdense coding and teleportation.

II. THEORY

A. Polarization rotation based on the PPLNOI

Figure 1(a) shows the structure of the PPLNOI ridge waveguide we utilize to manipulate the polarization entangled state. The device is fabricated by the following
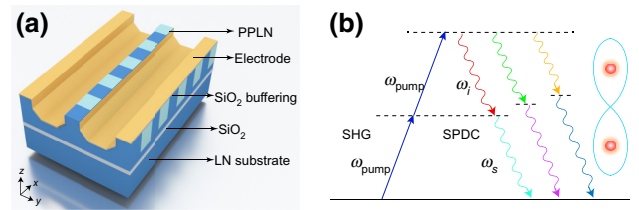

FIG. 1. (a) Structure of the PPLNOI ridge waveguide. (b) Schematic energy diagram for the cascaded SHG and SPDC processes.

procedures [37]: (1) bonding a PPLN chip with the predeposit silica layer on a LN substrate; (2) chemomechanical polishing of the bonded PPLN layer to thin the bonded PPLN layer to be 5.0 μm thick; (3) optical grade dicing to fabricate two parallel shallow grooves, forming a ridge waveguide with a dimension of 6.0 μm (width) $\times$ 5.0 μm (height) $\times$ 10 mm (length). Finally, a metal (Ni/Cr) electrode 50 nm thick is deposited on both side walls to form the transverse electrode, where the Ni layer is deposited between the Cr electrode and the side walls to make the electrode bonding on the PPLN layer better. To make the PPLN fulfill quasi-phase-matching (QPM) in the telecommunication band, the poling period Λ is designed to be 20.5 μm with a duty cycle of 50%. When a transverse (y-axis) electric field is applied along the waveguide, the optical axes of each of the positive and negative domains are alternately rearranged at small rocking angles of θ and $-\theta$ about the x axis with the form of $\theta \approx \gamma_{51}E/[(1/n_e)^2 - (1/n_o)^2]$ [38], where γ_{51} is the EO coefficient, and n_e, n_o are the extraordinary and ordinary refractive indices, respectively. At the QPM wavelength $\lambda = \Lambda(n_o - n_e)$, the polarization of the output is rotated by an angle of $2N\theta$ with respect to its horizontal (H) or vertical (V) initial state, where N is the domain number.

B. Cascaded SHG and SPDC processes based on the PPLN waveguide

Figure 1(b) shows an energy-level diagram of the cascaded SHG and SPDC processes as the pump photons and photon pairs are coupled via intermediate photons with frequency $\omega_m = \omega_{\text{pump}} + \omega_{\text{pump}} = \omega_s + \omega_i$, where m, s, and i represent the intermediate, signal, and idler photons, respectively, according to the energy conservation law. To achieve maximum conversion efficiency and high signal-to-noise rate, the phase-matching conditions for both of the two processes need to be simultaneously satisfied. Then, the quantum physics of this process can be described by the following effective Hamiltonian:

$$\hat{H} = \kappa \int_v dr^3 \chi_1 \chi_2 \hat{E}_p^{(+)}(r,t) \hat{E}_p^{(+)}(r,t) \hat{E}_s^{(-)}(r,t) \hat{E}_i^{(-)}(r,t)$$
$$+ \text{H.c.}, \tag{1}$$

where κ is the coupling constant related to the crystal, $E_n^{(+)}$ and $E_n^{(-)}$ $(n = p, s, i)$ are the positive- and negative-frequency component of the electric field operators, corresponding to the annihilation and creation operators, respectively. χ_1 and χ_2 are second-order susceptibility of the crystal for SHG and SPDC processes, respectively, and H.c. denotes a Hermitian conjugate. Following the model of SPDC in waveguide [39], one can express the spectral brightness, the down-converted signal power $d\mathcal{P}_s$ within a bandwidth $d\lambda_s$, for the cascaded SHG and SPDC processes as

$$\frac{d\mathcal{P}_s}{d\lambda_s} = \Gamma \chi_1^2 \chi_2^2 \mathcal{P}_p^2 \frac{1}{\mathcal{A}_{\mathrm{wg}}^2} \mathrm{sinc}^2 \left(\frac{\Delta k L}{2} \right), \qquad (2)$$

where $\mathcal{A}_{\mathrm{wg}}$ is the cross-section area of the waveguide, L represents the length of PPLN waveguide, $\mathcal{P}_p$ is the pump power, and Γ is the coupling constants related to idler and pump wavelength. Due to the high efficiency of SHG and low probability of SPDC process, only a small number of SH photons down-converted to photon pairs stimulated by vacuum fluctuations, which leads to a measurable SH wave at the output of the waveguide. Thus, one needs to suppress the remaining SH wave before using the photon pairs generated by the cascaded SHG and SPDC processes as the quantum source. For the SPDC process, only the nondegenerate part is useful because the degenerate photon pairs cannot be separated from the pump laser and suffer from strong noise. However, realizing simultaneous phase matching for the SHG and SPDC processes that can generate nondegenerate photon pairs covering a broadband spectrum is very challenging due to the dispersion in a medium. To ease this restriction, we take advantage of the type-zero QPM configuration and the weak dispersion property of PPLN in the telecommunication band.

III. EXPERIMENT AND RESULTS

Sagnac geometry has been widely used for generating polarization entanglement because it eliminates the need for stabilizing the interferometer and allows the biphoton output state to be easily controlled [40]. However, preparing fiber-based polarization entangled sources with a high spectral brightness is not easy because it is difficult for a fiber polarization beam splitter (FPBS) to operate at both wavelengths of fundamental wave and SH wave with no frequency dispersion and low insertion loss. To address these limitations, we develop a fiber-based hyperentangled source based on cascaded SHG and SPDC processes in a fiber Sagnac loop. The experimental setup of the hyperentangled source and the measurement setups are depicted in Fig. 2. A narrow-band cw laser (LTB-6728, Newport Corp.) at 1553 nm is passed through a dense wavelength division multiplexing filter (DWDM, ShenZhen Sharetop Technology Co., Ltd.) with an extinction ratio of 120 dB to suppress spontaneous emission noise. An optical circulator (CIR) is utilized to guide the pump laser into a fiber Sagnac interferometer, which consists of an in-line FPBS and a 5-cm-long PPLN waveguide. The normalized SHG efficiency of this waveguide is measured to be $\eta = P_{\mathrm{out}}/P_{\mathrm{in}}^2 = 450\%/\mathrm{W}$, where P_{in} and P_{out} correspond to the powers of the fundamental wave at the input and the generated SH wave at the output. In the interferometer, the pump laser is split into two orthogonal components and bidirectionally pumps the PPLN waveguide. To ensure the polarization of photons fulfills the type-0 phase-matching condition, the output fiber of the ordinary light side of the FPBS is rotated by 90°. Then, photon pairs are generated in the PPLN waveguide by the cascaded SHG and SPDC processes and recombined in the FPBS. By precisely controlling the polarization controller (PC), one can obtain the two-photon state after the CIR as $|\phi^+\rangle = \frac{1}{\sqrt{2}} (|H\rangle_i |H\rangle_s$
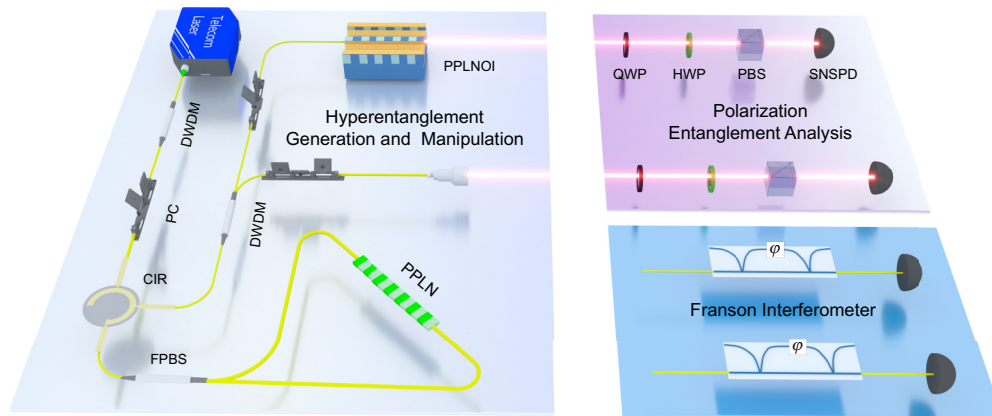

FIG. 2. Experimental setup for the generation and manipulation of hyperentanglement in polarization and time-energy DOFs. DWDM, dense wavelength division multiplexing filter; PC, polarization controller; FPBS, in-line fiber polarization beam splitter; CIR, circulator; QWP, quarter-wave plate; HWP, half-wave plate; PBS, cubic polarization beam splitter; SNSPD, superconducting single photon detector.
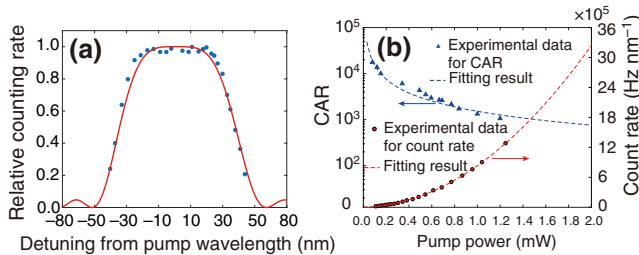
FIG. 3. (a) Spectrum of correlated photon pairs generated by cascaded SHG and SPDC processes. The blue points indicate experimental data while the red line is the theoretical result. (b) Experimental CAR and down-converted photon number under a different level of pump power.

$+ |V\rangle_i|V\rangle_s)$. To effectively suppress the pump laser, we use cascaded 100-GHZ DWDM filters with an extinction ratio of 120 dB to divert the signal and idler photons. The remaining SH wave generated in the Sagnac interferometer is also significantly suppressed by the CIR and DWDM filters.

First, we characterize the performance of the correlated photon pairs in terms of spectral bandwidth, brightness, and signal-to-noise ratio. The photons are detected by superconducting nanowire single-photon detectors (SNSPD, Photec Corp.) with the detect efficiency of over 80% and dark count rate of less than 40 per second. The detection events of the SNSPDs are recorded by a time-correlated single-photon counting (TCSPC, ID900-master, ID Quantique Inc.) and the coincidence window during the whole experiment is set to be 500 ps. Figure 3(a) shows the spectrum of correlated photon pairs of the source. The spectrum spans a full width at half maximum of approximate 60 nm, covering the whole telecom *C* band and *L* band. Then, we investigate the spectral brightness and signal-to-noise ratio of the source. The noises mainly include the spontaneous emission noise and spontaneous Raman-scattering noise of the pump laser. The former can be suppressed to a great extent by using a narrowband filter with a high extinction ratio before the laser is injected into the PPLN waveguide, while the later is hard to eliminate and grows with the pump power. Raman photons with wavelength nearby the pump wavelength are generated by the Raman Scattering in both the PPLN waveguide and fiber, making the SPDC photons inevitably contaminated by Raman photons. Fortunately, using a narrow-band filter to separate the SPDC photon pairs can keep the Raman-scattering noise mixed in the signal at a low level. The coincidence count to accidental coincidence count ratio (CAR) is the quality merit for characterizing the signal-to-noise ratio of photon pairs. In theory, CAR can be expressed as [41] $\mathrm{CAR} = \mathcal{C}\eta_i\eta_s/(\mathcal{C} + \eta_i\mathcal{D}_s)(\mathcal{C} + \eta_s\mathcal{D}_i)$, where $\mathcal{C}$ is the coincidence rate, η_n and $\mathcal{D}_n$, $(n = i, s)$ are the detect efficiency and dark count rate of the two

detectors. Figure 3(b) shows the experimental CAR and the detected single-channel photon number of the selected photon pairs under different pump levels. The red dashed line indicates the quadratic fit to the experimental data with the coefficient of determination R square of 0.9999, which strongly suggests that the down-converted signal photon number quadratically grows with the pump power and agrees reasonably well with the theory in Eq. (2). The source exhibits a high signal-to-noise ratio when keeping the photon rate at a high level and a CAR of higher than 18 000 is obtained with a photon-pair detection rate of 13.9 kHz. Thus, such a quantum source based on cascaded SHG and SPDC processes in a high-efficiency PPLN waveguide can be used in quantum-information tasks.

Next, we characterize the hyperentanglement in polarization and time-energy DOFs of the entangled source. A quarter-wave plate (QWP), a half-wave plate (HWP), and a cubic PBS are utilized for quantitative analysis of the polarized entanglement. By controlling the angle of the QWPs and HWPs, one can perform the projected measurements for the entangled states. To obtain the maximally entangled state, one needs to balance the photon-generation rate at the two circulation directions of the fiber Sagnac loop by precisely controlling the PC. In addition, the optical path difference between the clockwise and counterclockwise paths of the Sagnac loop needs to be within the coherence length of the SPDC photons, which is determined by the SPDC coherence time (about 10 ps due to the 100-GHz DWDM filter). Moreover, for the phase stabilization of the Sagnac interferometer, the total length of the Sagnac loop should not be very large so that the influences introduced by the environment on the clockwise and counterclockwise paths are the same [40]. In our experiment, the fiber length in the two sides of the PPLN waveguide is controlled to be 70 ± 1 cm. First, we perform the quantum-state tomography for the prepared state and reconstruct the density matrix by using the maximum-likelihood estimation [42]. The real and imaginary parts of the reconstructed density matrix are presented in Figs. 4(a) and 4(b), respectively, from which we calculate the fidelity to be $F = \langle\psi_{\mathrm{ideal}}|\rho|\psi_{\mathrm{ideal}}\rangle = 98.1\% \pm 0.3\%$. Using the standard coincidence measurement technique we record the two-photon interference fringes in terms of photon coincidence under two nonorthogonal projection bases, H/V and D/A (diagonal and antidiagonal). We fix the angle of the HWP of idler photons at 0 and $22.5°$, respectively, and measure the two-photon coincidence count as a function of the HWP rotation angle of signal photons. The experiment results are shown in Fig. 4(c). We obtain an average raw visibility to be $V = (\mathcal{N}_{\max} - \mathcal{N}_{\min})/(\mathcal{N}_{\max} + \mathcal{N}_{\min}) = 99.2\% \pm 0.4\%$. To further characterize the entanglement of the prepared state, we measure the S parameter of the Clauser-Horne-Shimony-Holt (CHSH) Bell inequality [43]. The maximum value of CHSH Bell inequality is obtained to be $S = 2.76 \pm$
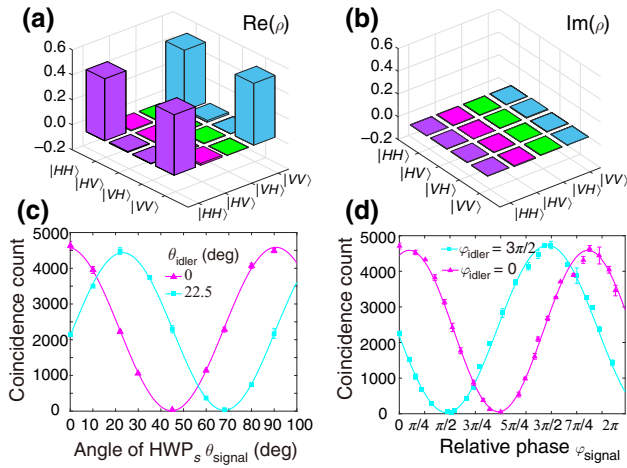
FIG. 4. (a),(b) Real and imaginary parts of the reconstructed density matrix for the polarization entangled state. (c) Two-photon coincidence count as a function of signal polarization under two nonorthogonal projection bases. (d) Franson-type interference patterns for observing time-energy entanglement.

0.03, which violates the inequality by 25 standard deviations. During the measurements of quantum-state tomography, two-photon interference and CHSH Bell parameters throughout our work, each coincidence count is repeated for 3 times to calculate the error bars with a single measurement time of 5 s. The results convincingly demonstrate that polarization entanglement is successfully prepared based on cascaded SHG and SPDC processes in a fiber Sagnac loop.

Time-energy entanglement is an inherent feature in photon pairs generated via cw laser pumped SPDC [44]. Owing to the narrow linewidth ($\Delta \nu < 200$ kHz) of the pump, a large emission time uncertainty ($\tau > 5$ μs) can be achieved during the SPDC process. Thus one can express the superposition state of the photon pairs emitted at different temporal mode as $|\psi\rangle = \kappa \int_0^\infty \xi(t)|t\rangle_s |t\rangle_i dt$, where κ is the coupling constant corresponding to the second-order susceptibility $\chi^{(2)}$ of the PPLN waveguide, and $\xi(t)$ is the emitted time-distribution function. The time-energy entanglement can be revealed by using a Franson-type interferometry [45]. If the relative path delay between the two arms of the interferometer is shorter than the coherence length of the pump, interference fringes can be observed by sweeping the relative phase of one interferometer. In our experiment, the Franson-type interferometer consists of two unbalanced Mach-Zehnder interferometers (MZIs, mint-1 × 2-band C-1 GHz, Kylia Inc.), which are made of free-space optical components and have an arm length difference of 1 ns in time domain. The relative phase between the two arms can be changed by applying the voltages to a resistive heater fixed on an optical element in the MZIs. The two-photon interference patterns under two nonorthogonal phase bases are measured by

sweeping the relative phase of signal MZI. The results are shown in Fig. 4(d). We obtain an average fringe visibility of $V = 98.5\% \pm 0.5\%$, which exceeds the nonlocal bound 71% of Bell inequality [10,43] and reveals a high quality of time-energy entanglement.

Entanglement manipulation is a key ingredient in quantum operations and becomes essential for distributed quantum-information tasks. Particularly in superdense coding, the precise manipulation of polarization entanglement is required to encode the four Bell states and accomplish the complete Bell-state measurement. Before demonstrating the conversion of the polarization entangled state, we first show the characteristics of precisely controlling the polarization state of our device with efficient and linear electro-optic tuning. In our experiment, the PPLNOI ridge waveguide (in collaboration with HC Photonics Corp.) has the capability of fast polarization rotation with a response speed over 100 MHz at a half-wave voltage of about 7 V [38]. The experimental setup is depicted in Fig. 5. A 500-fs pulse from a fiber mode-locked laser with a repetition frequency of 60 MHz passes through a thin-film DWDM filter and a fiber Bragg grating. As a result, we obtain a pulse laser at 1572 nm with a full width at half maximum of 0.2 nm. The laser is attenuated to weak coherent laser pulses with a mean photon number of 0.01 photon per pulse by a variable optical attenuator. Then, the single-photon pulses are injected into the integrated PPLNOI ridge waveguide to undergo polarization rotation controlled by the applied voltage from a arbitrary function generator. A PC and a FPBS are utilized to ensure the input photons are TM or TE polarized. To fulfill the QPM condition, the temperature of the waveguide is precisely controlled to be $72.0 \pm 0.01\,^\circ$C by the PID algorithm. A QWP, HWP, and cubic PBS are used to characterize the output polarization state by performing the projection measurements. Finally, the photons are detected by a (In, Ga)As single-photon detector (SPD, WT-SPD300-ULN, Beijing RMY Electronics Ltd.), which is triggered by the synchronic electric pulse signal from the mode-locked laser. The SPD has a quantum efficiency of 10% and a dark count probability of 1×10^{-6} per detect gate.

To fully demonstrate the characteristic to control single-photon polarization states of the PPLNOI waveguide, we preform the quantum-state tomography for the output polarization states. We choose the polarization state $|H\rangle$ and $|V\rangle$ as input states, and transfer them into quantum states $|V\rangle$ and $|H\rangle$, respectively. The input state is of high fidelity guaranteed by the FPBS with an extinction ratio of 24 dB, and the amplitude of the electric signal is set to be 7 V. We reconstruct the density matrices for the rotated quantum states using the maximum-likelihood estimation, with which we calculate the state fidelity. The experiment results are shown in Fig. 6, in which (a)–(c) and (d)–(f) are the reconstructed density matrices and experimental
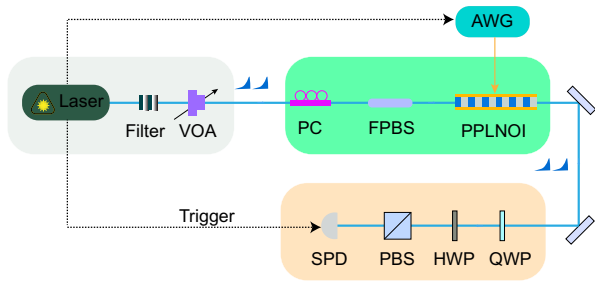
FIG. 5. Experimental setup of polarization manipulation of single photons on the PPLNOI ridge waveguide. VOA, variable optical attenuator; PC, polarization controller; FPBS, in-line fiber polarization beam splitter; AWG, arbitrary waveform generator; DWDM, dense wavelength division multiplexing filter; QWP, quarter-wave plate; HWP, half-wave plate; PBS, cubic polarization beam splitter; SPD, (In, Ga)As single-photon detector.

FIG. 7. (a) Two-photon coincidence counts as a function of signal polarization after entanglement manipulation. (b) Franson-type interference patterns for time-energy entanglement after entanglement manipulation.

Poincaré sphere for the output states $|V\rangle_{\text{out}}$ and $|H\rangle_{\text{out}}$ obtained after the $|H\rangle \rightarrow |V\rangle_{\text{out}}$ and $|V\rangle \rightarrow |H\rangle_{\text{out}}$ transformation, respectively. The average quantum-state fidelities are 99.7%, suggesting that our device can efficiently rotate the polarization state of single photons.

Then, we perform the polarization entanglement manipulation by utilizing the PPLNOI ridge waveguide, as shown in Fig. 2. The PPLNOI ridge waveguide can achieve fast and precise control of of single photons' polarization while preserving their linear polarization characterization. The signal photons from the hyperentangled source are injected into the PPLNOI ridge waveguide to undergo polarization rotation through the EO effect. When a transverse electric field is applied to the PPLNOI ridge waveguide, the two-photon entangled state will change as $|\phi\rangle_{\text{out}} = \frac{1}{\sqrt{2}}[|H\rangle_i(\alpha|H\rangle_s + \beta|V\rangle_s) + |V\rangle_i(\beta|H\rangle_s + \alpha|V\rangle_s)]$, where α and β are determined by the applied voltage to the PPLNOI waveguide with $\alpha^2 +$
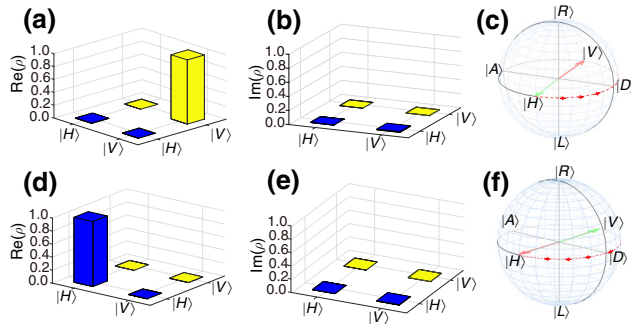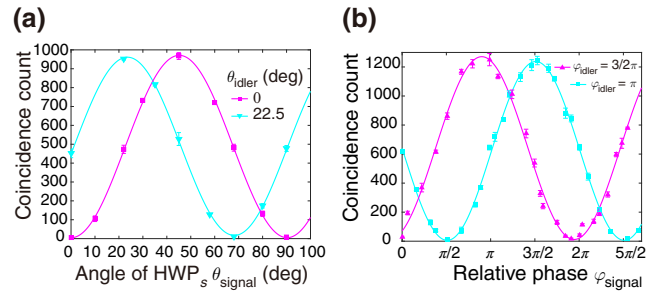

FIG. 6. (a),(b) and (d),(e) Experimental density matrices for the output single-photon states $|V\rangle_{\text{out}}$ and $|H\rangle_{\text{out}}$, respectively. (c),(f) Experimental Poincaré sphere for the output states $|V\rangle_{\text{out}}$ and $|H\rangle_{\text{out}}$ obtained after the $|H\rangle \rightarrow |V\rangle_{\text{out}}$ and $|V\rangle \rightarrow |H\rangle_{\text{out}}$ transformation, respectively. The red arrow lines represent the output polarization states while the green one indicates the input states.

$\beta^2 = 1$. When a electric field with the amplitude of half-wave voltage is applied to the PPLNOI, the entangled state $|\phi\rangle_{\text{out}}$ is transferred to another maximally entangled state $|\psi^+\rangle = \frac{1}{\sqrt{2}}(|H\rangle_i|V\rangle_s + |V\rangle_i|H\rangle_s)$. In general, only a local Pauli operation (σ_x, σ_y, σ_z) on the polarization degree of freedom of one of the photons is required to transform one maximally entangled Bell state to another [22], which can be achieved by appropriately setting an additional HWP and QWP [9]. To convert the state $|\phi^+\rangle$ to $|\psi^+\rangle$, we perform the operation σ_x to the polarization entangled state by applying the half-wave voltage of 7 V to the PPLNOI. The two-photon interference patterns after the polarization state conversion are shown in Fig. 7(a). The average raw visibility of the interference fringes are calculated to be $V = 97.8\% \pm 1.5\%$, revealing the high quality of the entangled state $|\psi^+\rangle$. In addition, we obtain the CHSH Bell parameter of $S = 2.74 \pm 0.04$, which violates Bell's inequality by more than 18 standard deviations. In our experiment, the PPLNOI acts as a high-speed HWP to rotate the polarization between H and V. When another PPLNOI or other high-speed polarization device like integrated lithium niobate EO modulator [36] are used to provide a phase shift of π between H and V, the polarization entangled state can be switched to the four ideal maximally entangled states $|\psi^+\rangle$, $|\psi^-\rangle$, $|\phi^+\rangle$, and $|\phi^-\rangle$ on demand. Due to the high-response speed of the PPLNOI waveguide, the polarization maximally entangled states can be fast switched to each other by using our PPLNOI, which may have great potential application in polarization-encoded quantum-communication tasks.

Another useful feature of polarization entanglement switching is maintaining the entanglement characteristics of other DOF during the conversion. To demonstrate this feature, time-energy entanglement of the photon pairs is measured by using the Franson-type interferometer as mentioned above. During the measurement, the amplitude of the electric filed applied to the PPLNOI waveguide is

set to be 7 V. Figure 7(b) shows the Franson-type interference fringes for time-energy entanglement after the polarization entangled state conversion, from which one can obtain average fitted visibilities of $V = 98.4 \pm 0.4\%$. The results convincingly imply that time-energy entanglement is well preserved during the polarization entangled-state modulation.

IV. DISCUSSION

Recently, quantum entanglement in time-energy, frequency-bin, and time-bin DOFs is, respectively, prepared by using the cascaded SHG and SPDC processes in a single PPLN waveguide [29], while we demonstrate hyperentanglement in polarization and time-energy DOFs through the same nonlinear processes in a fiber Sagnac loop. Similarly, we both generate the correlated photon pairs in a high-efficiency PPLN waveguide with a high spectral brightness and a large CAR. Compared with the work in Ref. [29], we achieve better visibility of the Franson-type two-photon interference for time-energy entanglement and higher fidelity of the entangled states. Our scheme can be used for high-dimensional quantum-communication tasks based on time energy and polarization hyperentanglement, like superdense coding over long-distance fiber link. In addition, it is worth noting that the fiber-based system can also operate in a pulsed scheme to generate and manipulate time-bin and polarization hyperentanglement. For the quality of entanglement, one needs to optimize the pump power to reduce the effects of multiple pair emission to the quantum interference according to the SPDC photon statistic properties [46], both in cw and pulsed schemes. During the superdense coding process, fast and precise manipulation of polarization entanglement is required to encode the four Bell states and accomplish the complete Bell-state measurement. In this case, one can take advantage of the characteristics of fast controlling the polarization entangled state of the PPLNOI waveguide to perform fast-encoding quantum tasks, such as fast superdense coding and superdense teleportation based on time-bin and polarization hyperentanglement.

On the other hand, there are still several points that need to be improved when using our system in practical application. First, although the two-photon interference is able to characterize the polarization and time-energy entanglement, performing the full quantum tomography of the polarization and time-energy hyperentangled state is essential in future quantum-information tasks. However, it is challenging to perform the full quantum tomography for time-energy entanglement due to the continuous-variable nature and the high-dimensional Hilbert space of time-energy entanglement. Second, the measurement system of polarization entanglement is not completely in fiber. One can use a piezoelectric polarization controller and FPBS to replace the wave plates and cubic PBS to perform the

projection measurements, which makes the measurement system completely in fiber and more compact in structure. Finally, it is difficult for the PPLNOI to rotate the polarization over a wide wavelength range at the same time and its modulation rate of EO polarization coupling needs to be improved.

V. CONCLUSION

In conclusion, we implement efficient generation and precise manipulation of hyperentanglement in polarization and time-energy DOFs. The hyperentanglement is generated by cascaded SHG and SPDC processes in a high-efficiency PPLN waveguide in a fiber Sagnac interferometer. The states achieve the two-photon interference visibility of higher than 99% for polarization entanglement, and achieve the Franson-type two-photon interference visibility of $V = 98.5\% \pm 0.5\%$ for time-energy entanglement. In addition, we succeed in controlling the polarization state switched from one maximally entangled state to another by utilizing a PPLNOI platform while the time-energy entanglement is well preserved during the manipulation. The high-performance system and fiber-based scheme can significantly reduce the complexity of quantum systems and serve as a quantum source for large-scale fiber quantum networks. In addition, we expect that our scheme has promising applications in quantum-information tasks, such as dense coding, superdense teleportation, and quantum cryptography on multiuser optical fiber networks.

[1] R. Horodecki, P. Horodecki, M. Horodecki, and K. Horodecki, Quantum entanglement, Rev. Mod. Phys. **81,** 865 (2009).

[2] J. T. Barreiro, N. K. Langford, N. A. Peters, and P. G. Kwiat, Generation of Hyperentangled Photon Pairs, Phys. Rev. Lett. **95,** 260501 (2005).

[3] F. Steinlechner, S. Ecker, M. Fink, B. Liu, J. Bavaresco, M. Huber, T. Scheidl, and R. Ursin, Distribution of high-dimensional entanglement via an intra-city free-space link, Nat. Commun. **8,** 15971 (2017).

[4] S. Ecker, P. Sohr, L. Bulla, M. Huber, M. Bohmann, and R. Ursin, Experimental Single-Copy Entanglement Distillation, Phys. Rev. Lett. **127,** 040506 (2021).

[5] J. T. Barreiro, T.-C. Wei, and P. G. Kwiat, Beating the channel capacity limit for linear photonic superdense coding, Nat. Phys. **4**, 282 (2008).

[6] B. P. Williams, R. J. Sadlier, and T. S. Humble, Superdense Coding Over Optical Fiber Links with Complete Bell-State Measurements, Phys. Rev. Lett. **118**, 050501 (2017).

[7] J. C. Chapman, T. M. Graham, C. K. Zeitler, H. J. Bernstein, and P. G. Kwiat, Time-Bin and Polarization Superdense Teleportation for Space Applications, Phys. Rev. Appl. **14**, 014044 (2020).

[8] T. M. Graham, H. J. Bernstein, T.-C. Wei, M. Junge, and P. G. Kwiat, Superdense teleportation using hyperentangled photons, Nat. Commun. **6**, 1 (2015).

[9] P. G. Kwiat, K. Mattle, H. Weinfurter, A. Zeilinger, A. V. Sergienko, and Y. Shih, New High-Intensity Source of Polarization-Entangled Photon Pairs, Phys. Rev. Lett. **75**, 4337 (1995).

[10] Q. Zhang, H. Takesue, S. W. Nam, C. Langrock, X. Xie, B. Baek, M. M. Fejer, and Y. Yamamoto, Distribution of time-energy entanglement over 100 km fiber using superconducting single-photon detectors, Opt. Express **16**, 5776 (2008).

[11] B. Brecht, D. V. Reddy, C. Silberhorn, and M. G. Raymer, Photon Temporal Modes: A Complete Framework for Quantum Information Science, Phys. Rev. X **5**, 041017 (2015).

[12] M. Malik, M. Erhard, M. Huber, M. Krenn, R. Fickler, and A. Zeilinger, Multi-photon entanglement in high dimensions, Nat. Photonics **10**, 248 (2016).

[13] A. Treiber, A. Poppe, M. Hentschel, D. Ferrini, T. Lorünser, E. Querasser, T. Matyus, H. Hübel, and A. Zeilinger, A fully automated entanglement-based quantum cryptography system for telecom fiber networks, New J. Phys. **11**, 045013 (2009).

[14] A. Barasiński, A. Černoch, and K. Lemr, Demonstration of Controlled Quantum Teleportation for Discrete Variables on Linear Optical Devices, Phys. Rev. Lett. **122**, 170501 (2019).

[15] S. M. Lee, S.-W. Lee, H. Jeong, and H. S. Park, Quantum Teleportation of Shared Quantum Secret, Phys. Rev. Lett. **124**, 060501 (2020).

[16] H.-S. Zhong, H. Wang, Y.-H. Deng, M.-C. Chen, L.-C. Peng, Y.-H. Luo, J. Qin, D. Wu, X. Ding, and Y. Hu, *et al.*, Quantum computational advantage using photons, Science **370**, 1460 (2020).

[17] S. Wengerowsky, S. K. Joshi, F. Steinlechner, H. Hübel, and R. Ursin, An entanglement-based wavelength-multiplexed quantum communication network, Nature **564**, 225 (2018).

[18] S. K. Joshi, D. Aktas, S. Wengerowsky, M. Lončarić, S. P. Neumann, B. Liu, T. Scheidl, G. C. Lorenzo, Ž. Samec, and L. Kling, *et al.*, A trusted node-free eight-user metropolitan quantum communication network, Sci. Adv. **6**, eaba0959 (2020).

[19] Y.-A. Chen, Q. Zhang, T.-Y. Chen, W.-Q. Cai, S.-K. Liao, J. Zhang, K. Chen, J. Yin, J.-G. Ren, and Z. Chen, *et al.*, An integrated space-to-ground quantum communication network over 4600 km, Nature **589**, 214 (2021).

[20] Y. Li, Y. Huang, T. Xiang, Y. Nie, M. Sang, L. Yuan, and X. Chen, Multiuser Time-Energy Entanglement Swapping Based on Dense Wavelength Division Multiplexed and

Sum-Frequency Generation, Phys. Rev. Lett. **123**, 250505 (2019).

[21] X. Liu, X. Yao, R. Xue, H. Wang, H. Li, Z. Wang, L. You, X. Feng, F. Liu, and K. Cui, *et al.*, An entanglement-based quantum network based on symmetric dispersive optics quantum key distribution, APL Photonics **5**, 076104 (2020).

[22] E. Y. Zhu, Z. Tang, L. Qian, L. G. Helt, M. Liscidini, J. E. Sipe, C. Corbari, A. Canagasabey, M. Ibsen, and P. G. Kazansky, Direct Generation of Polarization-Entangled Photon Pairs in a Poled Fiber, Phys. Rev. Lett. **108**, 213902 (2012).

[23] J. Suo, S. Dong, W. Zhang, Y. Huang, and J. Peng, Generation of hyper-entanglement on polarization and energy-time based on a silicon micro-ring cavity, Opt. Express **23**, 3985 (2015).

[24] S. Dong, L. Yu, W. Zhang, J. Wu, W. Zhang, L. You, and Y. Huang, Generation of hyper-entanglement in polarization/energy-time and discrete-frequency/energy-time in optical fibers, Sci. Rep. **5**, 9195 (2015).

[25] S. Arahira, N. Namekata, T. Kishimoto, H. Yaegashi, and S. Inoue, Generation of polarization entangled photon pairs at telecommunication wavelength using cascaded $\chi^{(2)}$ processes in a periodically poled LiNbO$_3$ ridge waveguide, Opt. Express **19**, 16032 (2011).

[26] Y. Jia, L. Wang, and F. Chen, Ion-cut lithium niobate on insulator technology: Recent advances and perspectives, Appl. Phys. Rev. **8**, 011307 (2021).

[27] Y. Zheng and X. Chen, Nonlinear wave mixing in lithium niobate thin film, Adv. Phys. X **6**, 1889402 (2021).

[28] T. Xiang, Y. Li, Y. Zheng, and X. Chen, Multiple-DWDM-channel heralded single-photon source based on a periodically poled lithium niobate waveguide, Opt. Express **25**, 12493 (2017).

[29] Z. Zhang, C. Yuan, S. Shen, H. Yu, R. Zhang, H. Wang, H. Li, Y. Wang, G. Deng, and Z. Wang, *et al.*, High-performance quantum entanglement generation via cascaded second-order nonlinear processes, npj Quantum Inf. **7**, 123 (2021).

[30] F. Dolde, V. Bergholm, Y. Wang, I. Jakobi, B. Naydenov, S. Pezzagna, J. Meijer, F. Jelezko, P. Neumann, and T. Schulte-Herbrüggen, *et al.*, High-fidelity spin entanglement using optimal control, Nat. Commun. **5**, 3371 (2014).

[31] K. Mattle, H. Weinfurter, P. G. Kwiat, and A. Zeilinger, Dense Coding in Experimental Quantum Communication, Phys. Rev. Lett. **76**, 4656 (1996).

[32] D. Bonneau, M. Lobino, P. Jiang, C. M. Natarajan, M. G. Tanner, R. H. Hadfield, S. N. Dorenbos, V. Zwiller, M. G. Thompson, and J. L. O'Brien, Fast Path and Polarization Manipulation of Telecom Wavelength Single Photons in Lithium Niobate Waveguide Devices, Phys. Rev. Lett. **108**, 053601 (2012).

[33] D. Turnbull, P. Michel, T. Chapman, E. Tubman, B. B. Pollock, C. Y. Chen, C. Goyon, J. S. Ross, L. Divol, N. Woolsey, and J. D. Moody, High Power Dynamic Polarization Control Using Plasma Photonics, Phys. Rev. Lett. **116**, 205001 (2016).

[34] Y. Cao, Y.-H. Li, W.-J. Zou, Z.-P. Li, Q. Shen, S.-K. Liao, J.-G. Ren, J. Yin, Y.-A. Chen, and C.-Z. Peng *et al.*

Bell Test Over Extremely High-Loss Channels: Towards Distributing Entangled Photon Pairs Between Earth and the Moon, Phys. Rev. Lett. **120**, 140405 (2018).

[35] K. Wei, W. Li, H. Tan, Y. Li, H. Min, W.-J. Zhang, H. Li, L. You, Z. Wang, and X. Jiang, *et al.*, High-Speed Measurement-Device-Independent Quantum Key Distribution with Integrated Silicon Photonics, Phys. Rev. X **10**, 031030 (2020).

[36] M. Zhang, C. Wang, P. Kharel, D. Zhu, and M. Lončar, Integrated lithium niobate electro-optic modulators: When performance meets scalability, Optica **8**, 652 (2021).

[37] T. Ding, Y. Zheng, and X. Chen, On-chip solc-type polarization control and wavelength filtering utilizing periodically poled lithium niobate on insulator ridge waveguide, J. Lightwave Technol. **37**, 1296 (2019).

[38] J. Wu, Y. Huang, C. Lu, T. Ding, Y. Zheng, and X. Chen, Tunable Linear Polarization-State Generator of Single Photons on a Lithium Niobate Chip, Phys. Rev. Appl. **13**, 064068 (2020).

[39] M. Fiorentino, S. M. Spillane, R. G. Beausoleil, T. D. Roberts, P. Battle, and M. W. Munro, Spontaneous parametric down-conversion in periodically poled KTP waveguides and bulk crystals, Opt. Express **15**, 7479 (2007).

[40] B. S. Shi and A. Tomita, Generation of a pulsed polarization entangled photon pair using a sagnac interferometer, Phys. Rev. A **69**, 013803 (2004).

[41] M. Collins, C. Xiong, I. Rey, T. Vo, J. He, S. Shahnia, C. Reardon, T. Krauss, M. Steel, A. Clark, and B. Eggleton, Integrated spatial multiplexing of heralded single-photon sources, Nat. Commun. **4**, 2582 (2013).

[42] D. F. James, P. G. Kwiat, W. J. Munro, and A. G. White, in *Asymptotic Theory of Quantum Statistical Inference: Selected Papers* (World Scientific, Singapore, 2005), p. 509.

[43] J. F. Clauser, M. A. Horne, A. Shimony, and R. A. Holt, Proposed Experiment to Test Local Hidden-Variable Theories, Phys. Rev. Lett. **23**, 880 (1969).

[44] P. G. Kwiat, A. M. Steinberg, and R. Y. Chiao, High-visibility interference in a bell-inequality experiment for energy and time, Phys. Rev. A **47**, R2472 (1993).

[45] J. D. Franson, Bell Inequality for Position and Time, Phys. Rev. Lett. **62**, 2205 (1989).

[46] H. Takesue and K. Shimizu, Effects of multiple pairs on visibility measurements of entangled photons generated by spontaneous parametric processes, Opt. Commun. **283**, 276 (2010).